Proceedings of the ASME 2022
International Design Engineering Technical Conferences and
Computers and Information in Engineering Conference
IDETC-CIE2022
August 14-17, 2022, St. Louis, Missouri

DETC2022-90582

COMPUTATIONAL DESIGN OF ADDITIVELY MANUFACTURED CURVILINEAR SCAFFOLDS FOR BONE REPAIR

David O. Cohen [1], Sohaila M. G. Aboutaleb[2], Amy Wagoner Johnson[2], Julian A. Norato[1,*]

[1]University of Connecticut, Storrs, CT
[2]University of Illinois at Urbana-Champaign, Urbana, IL

ABSTRACT

This work introduces a computational method for designing ceramic scaffolds fabricated via direct ink writing (DIW) for maximum bone growth, whereby the deposited rods are curvilinear. A mechanobiological model of bone adaptation is used to compute bone growth into the scaffold, taking into account the shape of the defect, the applied loading, and the density distribution of bone in which the scaffold is implanted. The method ensures smooth, continuously varying rod contours are produced which are ideal for the DIW process. The method uses level sets of radial basis functions to fully define the scaffold geometry with a small number of design variables, minimizing the optimization's computational cost. Effective elastic and diffusive properties of the scaffold as a function of the scaffold design and the bone density are obtained from previously constructed surrogates. These property surrogates are in turn used to perform bone adaptation simulations of the scaffold-bone system. Design sensitivities of the bone ingrowth within the scaffold are efficiently obtained using a finite difference scheme implemented in parallel. A demonstration of the methodology on a scaffold implanted in a pig mandible is presented. The scaffold is optimized to maximize bone ingrowth with geometric constraints to conform to the manufacturing process.

Keywords: bone scaffold, design, optimization, bone growth, curvilinear, direct ink writing

1. INTRODUCTION

Bone scaffolds are porous structures designed to offer an alternative to natural bone for use in bone grafting [1]. Bone grafting is a surgical procedure in which donor bone is implanted to replace bone that is too severely compromised to heal on its own [2]. This damage may be caused by trauma or disease, or may be congenital. In essence, a bone graft fills the damaged region, or the bone defect, providing the necessary support for new bone to grow [3].

*Corresponding author: julian.norato@uconn.edu

In the face of increasing demand, the current sources of graft material have serious limitations [4]. The preferred source is the patient, in which case the procedure is known as an autograft [3]. However, only so much material can be removed before the functionality of the donor bone is compromised, limiting their use to smaller defects [1, 5]. Moreover, autografts require that the patient undergo a surgery to remove the bone in addition to the implantation surgery, adding the potential for complications at the donor site [1, 5, 6]. The primary alternative to autografts are allografts. In an allograft, the source of bone is a donor other than the person receiving the graft [5]. Allografts only require a single surgery on the patient and are not subject to the same defect size restrictions as autografts. However, allografts are plagued by a shortage of donor material, and elevated risks of disease transfer and rejection by the patient [2, 5]. Moreover, both forms of graft are very expensive [7].

In light of the limitations of these two options, significant research efforts have been devoted to bone substitutes in recent years. Their clinical application remains limited, owing principally to difficulties in their design and manufacture [8]. This difficulty stems from the complex and frequently conflicting requirements any bone substitute must meet. Bone growth requires the growth of new blood vessels into the defect to facilitate the transport of nutrients, cells, and waste to and from the healthy bone surrounding the defect (the growth front) [9, 10]. Thus, to ensure that the defect fully heals, a certain level of porosity must be maintained by the scaffold. Simultaneously, a degree of mechanical compliance must be maintained, as bone growth typically requires stimulation in the form of mechanical loading to occur [9, 11]. Opposing these goals is the need for structural stability of the scaffold. Mechanical failure of the scaffold in vivo is not acceptable. Furthermore, excessive deformation impedes angiogenesis, slows the formation of bone, and results in a prolonged healing period [2, 12]. In vivo studies also suggest that too much local strain also affects cell differentiation at the defect site, favoring the formation of fibrous tissue over bone [13]. Adding to

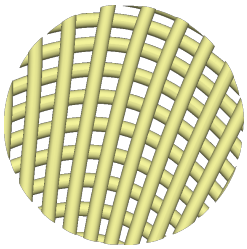

FIGURE 1: Top view of a computer-aided design (CAD) model of a curvilinear scaffold

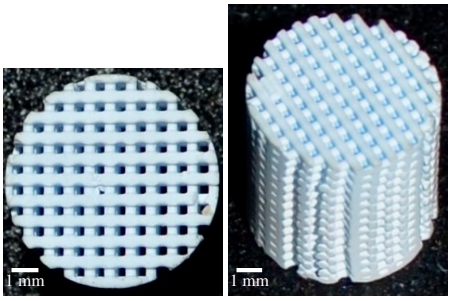

FIGURE 2: An 8mm diameter ceramic scaffold manufactured via direct ink writing (DIW) [35].

these requirements, as bone grows into the scaffold, the scaffold's properties change. Thus it is not guaranteed that a design which conducive to bone growth at implantation will remain so as time progresses [8].

Previous works have used computational optimization techniques to design the scaffold and attempt to address these challenges. Most of these works have focused on the mechanical properties of the scaffold (cf. [14–24]). The biological requirements of bone growth tend to be treated as structural constraints, if considered at all [8]. Several authors have employed transient finite-element-based mechanobiological simulations to investigate the effect of scaffold geometry on bone growth over time [10, 25–32]. In [10], a scaffold unit cell is optimized so that the rate of bone growth is matched to the rate of scaffold resorption. The goal is to ensure an adequate measure of mechanical stimulus and support is available throughout the bone growth process. Mechanobiological considerations are incorporated in the design of optimized scaffolds in [31], which focuses on the optimization of the rod diameter of a rhombicuboctahedral unit cell with the objective of maximizing bone growth before the combined bone-scaffold is so stiff that it inhibits further growth. [30] seeks to optimize a periodic unit cell for bone growth, subject to a constraint on scaffold compliance. This work incorporates analytical sensitivities of a transient bone growth model to perform gradient based topology optimization of the unit cell.

The authors of this paper recently formulated a computational design method for scaffolds fabricated via DIW and with rectilinear rods [32]. This method maximizes volume bone ingrowth while maintaining a specified level of stiffness at implantation. A transient mechanobiological simulation is used to determine bone growth in the scaffold from the time of implantation to a specified time. This simulation is subsequently used to create surrogates of bone growth and as-implanted stiffness as a function of scaffold design parameters. The scaffold optimization is then performed on these surrogates. This methodology is suitable for periodic scaffolds, as only a small number of design parameters is considered and thus the number of simulations required to construct the surrogate models is computationally feasible. However, for designs that require more parameters and offer potentially better growth performance, such as non-periodic designs arising from the use of curvilinear rods, the number of simulations needed to construct the surrogates makes the computational cost prohibitive.

In this paper, we build on our previous work by designing scaffolds with curvilinear rods, cf. Fig. 1. The directrices of the curvilinear rods are defined as level sets of an implicit surface defined using radial basis functions (RBFs). The advantage of this choice of geometric representation is that it can render a wide variety of curvilinear designs with a compact representation, i.e., with relatively few design variables. Moreover, the level sets of the RBF surface are smooth with the appropriate choice of basis function [33]. This facilitates the manufacturing of the scaffold by DIW by avoiding the need for abrupt changes in printing velocity and flow rate [34]. As in our previous work, the objective function consists of maximizing bone growth, which is evaluated via the mechanobiological simulation. The scaffold is treated as a homogenized solid, whose effective properties are extracted from surrogates built prior to the optimization using numerical homogenization and geometry projection techniques. The property surrogates are not only a function of the scaffold geometric parameters, but of the amount of bone growth. Therefore, the effective properties at a given location within the scaffold and at a given time are a function of the local scaffold geometry and the amount of bone ingrowth from the previous time step. We employ a finite difference scheme to efficiently compute design sensitivities so that we can employ efficient gradient-based optimizers for the design. This scheme is implemented using parallel computing for efficiency. Thanks to the compactness of our curvilinear design representation, the proposed method can simultaneously perform the primal mechanobiological simulation and all the simulations corresponding to individual perturbations of the design parameters needed to compute the design sensitivities. The proposed method also imposes geometric constraints in the optimization to ensure the optimized scaffold design is manufacturable via DIW.

The rest of this manuscript is organized as follows. Section 2 and Section 3 present the details of the formulation and the computational implementation, respectively. Section 2 describes the formulation of the proposed method, including the definition of curvilinear geometry, the geometric constraints, and an overview of the bone growth model. Section 3 presents details of the computer implementation, including the parallel computation of finite difference sensitivities. The proposed method is demonstrated through the design of a scaffold in a pig mandible in Section 4. We present our conclusions from this work in Section 5.

2. FORMULATION

The details of portions of the formulation, including the mechanobiological simulation and the construction of effective property surrogates, are largely identical to those employed in our previous work [32]. As such, this section only discusses those elements of the formulation at a high level for brevity, and provides a detailed exposition for the novel aspects of the proposed method.

2.1 Scaffold Geometry

2.1.1 Geometric representation requirements. We start our formulation by describing how we represent the curvilinear scaffolds. While our representation can potentially accommodate other processes, it is tailored DIW fabrication. In DIW, the scaffold is constructed from biocompatible ceramic inks using robotic deposition techniques. This method works by extruding and depositing a colloidal ceramic suspension, or ink, out of a robotically positioned nozzle [36]. While extrudable, the suspension maintains its shape and can bridge small gaps without the aid of support material. The shape of the scaffold is then built up layer by layer, similar to conventional fused deposition modeling (FDM) printers for plastics. To ensure a bond between alternating layers, they are printed such that the rods overlap by some amount, which can be controlled in the manufacturing. Once the structure is complete, the part is sintered. When sintered, overlaps between rods form fully fused joints. A rectilinear scaffold fabricated in this manner is shown in Fig. 2. We assume that the distortion of the rod cross sections at rod intersections is negligible, and that the rods are of a uniform circular cross-section. Moreover, we restrict our efforts to scaffolds whose layers are planar; that is, the rod height within a layer is constant.

To optimize curvilinear scaffolds, a suitable mathematical representation is necessary. Ideally, such a representation would be compact, requiring a small number of design variables to control the geometry without unduly restricting the design space. This compactness enables a feasible computational cost for the optimization. Furthermore, the representation must accommodate the necessary manufacturability and biological constraints. The DIW process cannot accommodate rods on the same layer intersecting, either with themselves or other rods. Of particular importance is the rod center-to-center spacing l (see Fig. 5) within a layer. During fabrication, this spacing cannot exceed a certain maximum size or the unsintered rods will sag. After implantation, the rod spacing cannot be too small or tissue will not be able to grow into the scaffold. Therefore, l must be readily computed from the geometric representation everywhere within the scaffold. Futhermore, any design representation must define the contours of two rod layers. Curvilinear scaffolds are composed of repetitions of two complimentary layers that we shall refer to as the primary and alternate. Fig. 3 shows the primary and alternate layers of the scaffold from Fig. 1. The rods of these two layers need to run across each other, tying the scaffold rods together into a unified structure. The rods of primary and alternate layers should preferably be perpendicular to each other at their intersections. This requirement is motivated by the fact that for a given level of overlap between adjacent layers, perpendicular intersections of rods minimize the amount of surface area lost to the intersection. This is undesirable since bone requires exposed surface to grow on [9]. Since bone defects have irregular shapes, the final requirement on the geometric representation is that it should conform to arbitrary shapes.

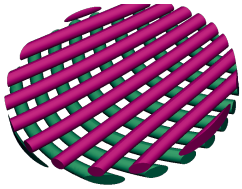

FIGURE 3: Two layers of a curvilinear scaffold with the primary rod layer colored blue-green and the alternate layer colored in magenta

2.1.2 Radial basis function interpolants. A represention of the scaffold via level sets of a surface constructed using 2D RBF interpolants satisfies the requirements outlined in the previous section. A radial basis function interpolant can be defined as

$$f(\mathbf{u}) = p_0 + \mathbf{p}^T \mathbf{u} + \sum_{i=1}^{n} w_i \phi(d(\mathbf{c}_i, \mathbf{u})), \tag{1}$$

where ϕ is a radial basis function, and $d(\mathbf{c}_i, \mathbf{u})$ is a suitable measure of distance between the evaluation point $\mathbf{u}$ and $\mathbf{c}_i$ is the center of the ith RBF. For this paper, $d(\mathbf{c}_i, \mathbf{u})$ is the L^2 norm, and ϕ is the thin-plate spline $\phi(r) = r^2 \ln(r)$[33]. The values of p_0, $\mathbf{p}$, w_i in 1 are constants determined by the fitting process, and n is the number of RBFs used by the interpolant. The procedure for calculating these constants to fit the interpolant will not be discussed here for brevity, but can be found in the literature cf. [37, 38].

To derive the curved scaffold rods from the interpolated surface, we use its level sets. Each rod on the primary layer of the scaffold corresponds to a contour on the level set of the interpolant's surface. The design variables for this parameterization correspond to the center points and heights that the interpolant is fitted to. The directrix of each curvilinear rod thus corresponds to a level set of this surface, with level sets corresponding to $f(\mathbf{u}) = k\lambda,\ k = 1, 2, \cdots$, where λ is a specified value.

This representation is compact; in the scaffold shown in Fig. 4, for example, 16 rods in 2 layers are defined by only 12 variables. This is in contrast to Bézier curves or splines, which would require at least 4 variables for each rod in the primary layer. This level-set representation naturally produces contours that are free of intersections without the need for additional constraints. Such constraints would be required if, for example, Bézier or spline representations were used for each rod. Another advantage of the RBF representation is that the level sets are smooth and therefore easy to fabricate in the DIW process. This smoothness owes to the minimal-energy property of thin plate RBFs. The RBF representation is also adaptable, in that as many RBFs as desired may be added to the interpolant, allowing for more complex level sets to be created and consequently providing more design freedom.

The separation between rods for the RBF representation is

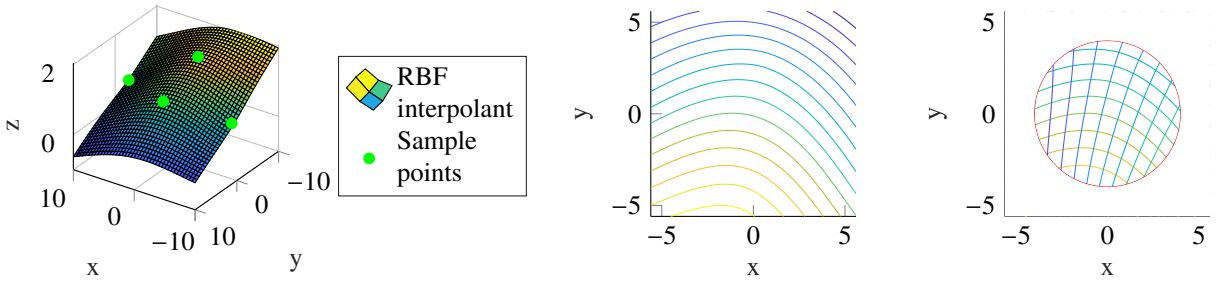

(a) RBF surface **(b)** Level sets **(c)** Final scaffold design

FIGURE 4: An RBF interpolant is fitted so that it attains the values h_i at the center points $\mathbf{c}_i$, creating a surface like the one shown in Fig. 4a. The rod directrices correspond to level sets of the surface, as shown in Fig. 4b. Curves orthogonal to these level sets are then generated numerically to generate the alternate layer, and the resulting contours are cut to the final scaffold shape as shown in Fig. 4c

readily computed as

$$l(\mathbf{u}) = \frac{\lambda}{\|\nabla f(\mathbf{u})\|}, \tag{2}$$

which follows from the first-order Taylor series approximation of the signed distance function, and where the interpolant gradient can be derived from 1 as

$$\nabla f(\mathbf{u}) = \mathbf{p} + \sum_{i=1}^{n} w_i \frac{\partial \phi}{\partial r}(d(\mathbf{c}_i, \mathbf{u}))\nabla d(\mathbf{c}_i, \mathbf{u}). \tag{3}$$

Finally, the level sets for the alternate layer must also be found. Unfortunately, this cannot be done analytically, but they can be easily obtained numerically. To ensure the rods of the alternate layer are perpendicular to the primary layer rods at all points, we define a function g such that $g_x = -f_y$ and $g_y = f_x$.. To obtain g, we employ numerical techniques to reconstruct a surface from a gradient field (cf. [39]). Since ∇g must be approximately equal to the finite difference of g, we can construct a system of equations solving for g at a set of points. This leads to an overdetermined system that is solved using least squares. Once g is solved for, its level sets can be used to define the alternate layer. An example of a completed scaffold design with its alternate layer is shown in Fig. 4c.

2.2 Bone growth model

As previously mentioned, bone requires a certain amount of load or stimulus as well as an adequate supply of osteoblasts to grow. Osteoblasts are the cells which specialize in the repair and maintenance of bone, which are responsible for the actual growth process [9]. However, as new bone is deposited, the distribution of stresses in the bone and ease of fluid transport (i.e. diffusivity) change even under a constant stimulus. This means modeling the transient bone growth is required to characterize the performance of a scaffold. The bone growth model adopted in this work is based on that of [9, 26, 40]. In a previous work, we adapted this model to predict bone growth in rectilinear scaffolds [32].

This model uses strain energy density as a measure of mechanical stimulus, and diffusion as a model of cell transport. Based on the mechanical stimulus received and the relative concentration of cells at a point, the bone deposited there is estimated. The bone growth model consists of a finite element-based simulation that estimates the density change in bone on an element-wise basis. The bone is assumed to have an infinite supply of osteoblasts that is not depleted by the bone growth process. A linear static analysis on the bone-scaffold assembly is performed to determine the stress distribution, and a transient mass diffusion analysis is conducted to determine the concentration of osteoblasts in each element. At every time step during the healing period, the density and material properties of each element are updated.

The analysis region Ω is separated into two domains: scaffold (Ω_s) and bone (Ω_b), with $\Omega = \Omega_s \cup \Omega_b, \Omega_s \cap \Omega_b = \emptyset$. The bone domain contains all of the pre-existing bone surrounding the scaffold. The scaffold domain consists of the scaffold itself, and any bone that grows within it. The material properties of the two domains are calculated differently. Any elements in the bone domain are henceforth referred to as bone elements, and any in the scaffold domain as scaffold elements. The calculations pertaining to these domains are detailed in [32] and are not repeated here. However, the density update, which we now describe, is the same for both regions.

As the density update is done on each element, we compute all relevant local quantities at the element centroid and assume they are uniform within the element. Therefore, while the expressions shown in the following can be computed at any point $\mathbf{x} \in \Omega$, in the implementation they are computed at each element centroid. The density for each time step is computed using the update

$$\rho_{t+\Delta t}(\mathbf{x}) = \min(\hat{\rho}_b,\ \rho_t(\mathbf{x}) + \dot{\rho}(\mathbf{x})\Delta t), \tag{4}$$

where $\rho_{t+\Delta t}$ and ρ_t denote the bone density at times $t + \Delta t$ and t, respectively, and $\hat{\rho}_b$ is the maximum possible density of bone. This density is based on empirical measurements of bone density. A small minimum allowable bone density $\tilde{\rho}_b$ is also imposed everywhere to ensure the mechanical properties of bone are not zero, which leads to an ill-posed mechanical analysis, and leads to a division by zero in the growth model (cf. [32]). we thus assign $\rho_0 = \tilde{\rho}_b$ for all $\mathbf{x} \in \Omega_s$. Both $\tilde{\rho}_b$ and $\hat{\rho}_b$ can be found in [32].

The rate of change in bone density $\dot{\rho}(\mathbf{x})$ is computed at each

time step as [26]

$$\dot{\rho}(\mathbf{x}) = S_{eff}\, S(\mathbf{x})\dot{r}(\mathbf{x})\hat{\rho}_b, \tag{5}$$

where S is the specific surface area in element e. S_{eff} is an empirical constant that represents what fraction of the available surface area actually supports bone growth. S is calculated differently for the bone and scaffold domains due their differing microstructure. Likewise, S_{eff} attains different values for the two regions. $\dot{r}(\mathbf{x})$ is the rate of bone deposition, calculated based on the mechanical stimulus and osteoblast concentration at point $\mathbf{x}$. Note that we assume bone resorption is negligible over the growth period, so $\dot{\rho}(\mathbf{x}) \geq 0$. The formulas for each of the quantities in (5) can be found in [32].

2.3 Scaffold properties

In order to perform the elasticity and diffusion analyses required by the growth model, scaffolds properties must be incorporated into the finite element model. As the structural details of the scaffold are small relative the scale of the bone, a conforming mesh of the scaffold geometry would require many elements and add considerable computational expense. To avoid this, the scaffold is instead modeled as a homogenized bulk material, whose properties are applied to the elements in the scaffold region (cf. [32]). This is complicated by the spatially variable scaffold geometry, which implies spatially varying homogenized properties. Our approach to this problem is to assume that locally the properties of the curvilinear scaffold can be approximated by a rectilinear scaffold unit cell. Essentially, at the centroid of every element, we determine the approximate rectilinear unit cell parameters and orientation. This information, combined with the in-grown bone density, is then used to determine the scaffold properties at that element. In our previous work on rectilinear scaffolds, we created a surrogate model of the scaffold properties as a function of its geometric parameters. The effective properties for each design used in the construction of the surrogate are obtained by numerical homogenization of a periodic unit cell. Geometry projection techniques are used so that the analyses for the numerical homogenization can be performed on a non-conforming mesh so as to circumvent remeshing. For brevity, details of the surrogate construction are not provided here, and the interested reader is referred to [32].

The surrogate model returns the elastic and diffusion properties as a function of the in-grown bone density ρ_b and two dimensionless constants d/l and $\alpha := 1 - a/d$. a, d, and l are as defined in Fig. 5. In general, higher d/l and α correspond to stiffer unit cells with less interstitial space. d is effectively a fixed value, determined by the nozzle size of the DIW machine and the shrinkage caused by the sintering process. The layer offset a is in general independent of the curvilinear rod layout and thus α is a design variable. As previously shown, l can be found from the radial basis function representation via 2.

To appropriately rotate the scaffolds properties, the local unit cell orientation (θ in Fig. 5) must be determined. We take the convention that the local y-axis of the unit cell at any point in the scaffold is oriented along the gradient of interpolant at that point. Therefore, the unit vector $\mathbf{n}$ of the unit cell orientation can be found by normalizing the gradient:

$$\mathbf{n} = \frac{\nabla f}{\|\nabla f\|}, \tag{6}$$

from which the unit cell orientation θ can be readily calculated.

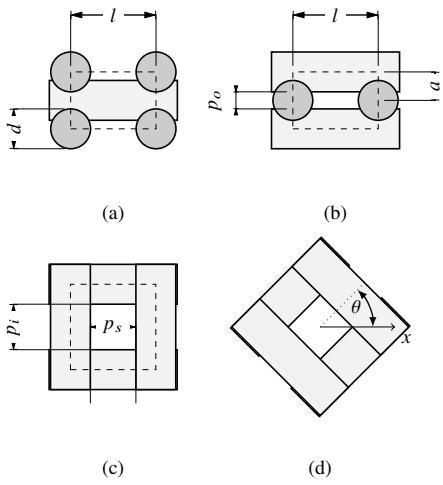

FIGURE 5: Unit cell of the rectilinear scaffold (enclosed by dashed lines) with rods shown in gray. z is the direction perpendicular to the deposited layers, and θ is the orientation about the z axis. The out-of-plane cross sections (a) and (b) are perpendicular to the xy plane and to each other. The in-plane cross-section (c and d) is normal to the z axis. θ also corresponds to the angle between the axes of the rods in alternating layers and the x and y axes, respectively.

2.4 Objective function

The design goal in our method is to maximize bone ingrowth. The best way to quantify bone growth in scaffolds is still an open question. One metric used in the literature is mass bone growth, defined as [26]

$$m_f := \frac{\int_{\Omega_s} \rho_t(\mathbf{x})|_{t=t_f}\, dv}{\int_{\Omega_s} \hat{\rho}_b\, dv} \approx \frac{\sum_{e\in\Omega_s} \rho_e|_{t=t_f}\, v_e}{\sum_e \hat{\rho}_b v_e}. \tag{7}$$

Full osteointegration for mass bone growth (i.e., a mass fraction of 1) would imply that fully dense bone fills all the interstitial space within the scaffold. However, a more clinically relevant definition may be to require that bone occupies the entire scaffold, but not necessarily at the maximum density. The latter definition is more consistent with the fact that the bone itself is not fully dense everywhere.

2.5 Fill fraction constraint

To ensure the manufacturability of the final scaffold design, an additional constraint beyond those on the rod center-to-center spacing l must be imposed. When the DIW process deposits a new rod over existing rods, it displaces some material in both the new and existing rods. How much material is displaced depends on the overlap α. Too large of an intersection can cause the pores between rods to be filled in by the displaced material. Rod layouts

with low d/l values are not affected by this problem, since there is more space for the displaced material to occupy. To predict this behavior, we formulate a scaffold fill fraction defined as

$$q = \frac{V_{Int}}{V_{RVE}}, \tag{8}$$

where V_{Int} is the total volume of the rod intersections in a unit cell, and V_{RVE} is the volume of the unit cell. V_{Int} can be computed as [41]:

$$V_{Int} = 2(1-\kappa)v_{Int}, \tag{9}$$

where v_{Int} is the volume of one complete rod intersection at a right angle with coplanar axes, (i.e. a Steinmetz solid) and κ is an adjustment factor that accounts for the separation between the cylinder axes. The factor of 2 reflects the fact that there are two full intersections per unit cell. The volume of a Steinmetz solid is $v_{Int} = 16r^3/3$, where r is the rod radius. κ can be found via [41] as

$$\kappa = 1 - (1+\eta^2)(1+\eta)E(m) + 2\eta(\eta+1)K(m). \tag{10}$$

In this expression, $K(m)$ and $E(m)$ denote the complete elliptic integrals of the first and second kind. Note that there are two definitions of these integrals in common use, one in which the argument m is squared in the integral, and one where it is not; we use the latter. m is computed as

$$m = \left(\frac{1-\eta}{1+\eta}\right)^2, \tag{11}$$

where $\eta = a/r$, where a is as defined in Fig. 5 and r is as defined earlier. For a fixed maximum fill fraction, this constraint effectively links l and a. If l is large, a can be close to the rod radius since the volume of the intersections is smaller relative to the total unit cell size. If l is small, then a must be large relative to the rod radius.

2.6 Optimization problem statement

Bringing together the objective and constraints discussed in previous sections, the optimization problem we seek to solve is

$$\begin{aligned}
&\max_{\mathbf{c},\mathbf{h},\alpha} \quad m_f(\mathbf{c},\mathbf{h},\alpha) \\
&\text{subject to} \\
&\widetilde{\max_{\mathbf{x}\in\Omega_p}} \quad \frac{l(\mathbf{c},\mathbf{h},\mathbf{x})}{l_{max}} - 1 \le 0 \\
&\widetilde{\max_{\mathbf{x}\in\Omega_p}} \quad 1 - \frac{l(\mathbf{c},\mathbf{h},\mathbf{x})}{l_{min}} \le 0 \\
&\widetilde{\max_{\mathbf{x}\in\Omega_p}} \quad \frac{q(\mathbf{c},\mathbf{h},\alpha,\mathbf{x})}{q_{max}} - 1 \le 0 \\
&\alpha_{min} \le \alpha \le \alpha_{max} \\
&c_{min} \le c_{ix} \le c_{max} \\
&c_{min} \le c_{iy} \le c_{max} \\
&h_{min} \le h_i \le h_{max},
\end{aligned} \tag{12}$$

where $\mathbf{c}$ is the vector of the x- and y-coordinates of the interpolant center points, and $\mathbf{h}$ is the vector of heights at those points. α is the unitless overlap fraction defined in 2.3. As we regard the rod diameter d as fixed, this variable effectively controls a. $\widetilde{\max}$ is a smooth approximation of the maximum, used to ensure differentiability and enable the use of efficient gradient-based optimizers. Here, we employ the Kreisselmeier-Steinhauser function for $\widetilde{\max}$. It is important to note that the constraints are applied over the region Ω_p, corresponding to the printed domain. This domain includes Ω_s as defined in Section 2.2, but also regions that are printed but removed when the scaffold is machined to its final shape. These regions were included in the constraint because print failures in these regions can propagate to Ω_s and ruin the print.

3. IMPLEMENTATION

To demonstrate our methodology, we optimize an 8 mm diameter scaffold implanted in six different locations in a pig mandible. We compare the optimized design of the curvilinear scaffold to a) a rectilinear scaffold for the same application, which was optimized using the previously reported methodology in [32] (see Fig. 9a); and b) to a design that has been used in experimental studies [42] (see Fig. 9b). For the curvilinear scaffolds, the level set surface was defined using 4 RBFs. The center point coordinates, the center point heights and the rod overlap α provided the optimizer with a total of 13 design variables.

3.1 Bone Adaptation Model

The mechanobiological simulation requires the strain energy density within the bone and scaffold at every point, as well as the normalized osteoblast concentration (cf. Section 2.2). These quantities are obtained from linear elasticity and transient diffusion finite element analyses of the pig mandible with the implanted scaffold. Both analyses were performed using an in-house code based upon the deal.ii finite element library [43]. The deal.ii library facilities for scalable distributed memory parallelization were employed for efficient utilization of all available CPU cores. The AztecOO package of Trilinos was used as the solver for the ensuing system of linear equations via the built-in interface available in deal.ii [44].

The voxelized, non-conforming mesh of the bone and scaffold regions was created using Hypermesh [45] and it is entirely composed of linear hexahedral elements. The bone update procedure is implemented as part of the analysis code. The rotation of the local scaffold properties due to the curvature of the rods is achieved by rotating the elasticity tensor of the homogenized scaffold material within the finite element code. For the diffusion analysis, the bone region surrounding the scaffold is treated as a source of osteoblasts, with a fixed normalized concentration of 1. The scaffold region is assumed to have a zero initial osteoblast concentration at implantation [26]. Note since the scaffold is treated as a homogenized material, the mesh does not change for different design parameters, and only the properties of the scaffold region elements are changed.

Most of the constants required for the bone growth simulation are the same as those used in [32], except for the reference mechanical stimulus value Ψ^* and the lazy zone width w. The

former is the mechanical stimulus threshold above which the bone will grow and below which bone will be resorbed [9]. The latter is a range of the stimulus value around Ψ^* within which negligible bone adaptation will occur. To estimate what this value would be for the pig mandible, we assumed that the mandible's existing bone density is perfectly adapted to the loads it experiences. Therefore, the stimulus it sees as part of a standard mastication cycle should be approximately equal to Ψ^*. To find this stimulus value, experimentally measured strains from a study of pig mastication [46] were used to estimate the reference stimulus, approximately 10 MPa/day.

In regards to the determination of the lazy zone width w, several authors have simply set this value to some percentage of the reference stimulus. In [9], it is set to 25%; in [40], to 10%. We opted to use the former, which corresponds to a value of w of 2.5 MPa/day.

3.2 Computation of sensitivities

We wish to employ efficient gradient-based methods for the optimization. Gradient-based methods were selected over global optimization methods because of the cost of the bone-growth simulation, which would make the optimization via zero-order methods impractical. While it is possible to compute analytical sensitivities for our bone growth model (see, for example, [30]), a simpler and faster approach that is enabled by the compact design representation is to use first-order backward finite differences to approximate the design sensitivities. To do this efficiently, a Python framework was implemented that creates a set of perturbed designs around the current design. Bone growth simulations of these perturbed designs are performed in parallel on a high performance computing system, with each simulation running on one compute node. In turn, each individual simulation is performed in parallel using all the available cores in the node where it is running. Through the techniques and interfaces available in the deal.ii library, domain decomposition and parallel linear algebra utilities are employed to perform the analysis. After all the simulations are completed, the Python framework collects the mass growth values, computes the design sensitivities using finite differences, and passes these data to the optimizer. The SLSQP routine from SciPy [47] is employed for the optimization .

This parallel finite difference approach can actually be more efficient in terms of wall-time than analytical sensitivities provided there are enough computing resources available to perform all the perturbed design analyses simultaneously. This is because analytical sensitivities for a finite element model are usually calculated via the adjoint method, which requires an additional analysis be performed after each time step to compute the adjoint solution. This adjoint analysis usually requires a similar amount of time as the primal analysis, roughly doubling the wall time per iteration. The parallel finite difference method, on the other hand, allows a simultaneous execution of the analyses necessary to compute the objective function and its sensitivities, and thus suffers no such penalty. It is important to note that this benefit is only realized if all the simulations can be executed in parallel, which may not feasible depending the problem and available computational power.

The use of sensitivities and the associated gradient-based optimizers introduced the possibility of the optimization getting trapped in poor local minima. To minimize this risk, the optimization was run from 8 different starting points. These points were selected by conducting a large random sampling of the design space, with geometrically infeasible designs discarded from the sample. The designs that exhibited the largest standard deviation of d/l ratios across the scaffold domain (i.e., those that were the least rectilinear) were chosen as starting candidates. To ensure all the starting designs were not too similar to each other, the candidate designs were visually inspected.

3.3 Constraints

A summary of the variable bounds and constraint values is shown in Table 1. As our goal is to produce scaffolds fabricated via DIW, we seek to impose physically realistic constraints based on the capabilities and limitations of the manufacturing process. For the following, we used a printing nozzle diameter of 610 μm. The shrinkage due to sintering was found to be a approximately 20%.

Variable	Description	Value
h_{min}	Min. height	-2
h_{max}	Max. height	2
c_{min}	Min. center point coordinate	-10
c_{max}	Max. center point coordinate	10
l_{min}	Min. rod center-to-center spacing	610 μm
l_{max}	Max. rod center-to-center spacing	1528 μm
q_{max}	Max. fill fraction	0.173
α_{min}	Min. rod overlap fraction	0.05
α_{max}	Max. rod overlap fraction	0.3975

TABLE 1: Constraint values and design variable bounds

The lower limits imposed on α reflect the requirement that the rods of each layer must have at least some overlap with those of the previous layer to ensure joint fusion. The DIW process effectively deposits the rods in tension, giving them the ability to span gaps. However, this can also cause previously printed rods to be pulled out of place if they are not sufficiently well bonded with the previous layer. We impose a lower bound α_{min} = 0.05 to address these requirements. The upper bound of α arises from the need to ensure a minimum out-of-plane pore size (p_o in Fig. 5). As previously mentioned, this ensures sufficient space for vascularization and to facilitate tissue in-growth. We set a minimum pore size of 100 μm in any direction (as-sintered). For the pore size along the build direction, this translates to α_{max} = 0.3975.

As previously mentioned, l cannot exceed a maximum value before rod sagging during the deposition becomes excessive. This limit was found experimentally to be 1910 μm, which translates to a sintered l_{max} of 1528 μm. The lower limit of l is dictated by the maximum allowable d/l value of 0.8, which corresponds to the largest rod diameter-to-rod separation ratio considered in the construction of the surrogate model for the scaffold properties. This translates to l_{min} = 610 μm. A maximum fill fraction q_{max} of 0.173 was conservatively estimated by calculating the largest fill fraction of several designs that are known to be printable.

The coordinates of the interpolant center points in the xy plane are bound to the $[-10, 10]$ range to keep them within a reasonable distance of the origin. This is desirable because points that are far from the scaffold origin would have almost no effect on the level set surface, which could cause RBFs to be effectively "lost" by the optimizer. Bounds $h_{min} = -2 \leq h_i \leq h_{max} = 2$ on the heights are also imposed, since excessively large differences in heights between points result in steep surfaces with rod spacings that are too small.

3.4 Methods

The mandible geometry was extracted from a CT scan of an adult pig using Amira [48]. Six circular defects were created in the mandible, each 8 mm in diameter, as shown in Fig. 6. Each scaffold is assigned a code to identify it, as shown in Fig. 7.

FIGURE 6: Isometric view of the mandible geometry. The scaffold regions are shown in grey.

3.4.1 Finite Element Model. The mechanobiological simulation requires the initial bone density distribution of the bone surrounding the implants. The initial bone density distribution for the mandible was derived from CT scan data in the same manner as in our previous work [32]. These values were then mapped to the mesh bone region by assigning to each element the density of the CT scan voxel closest to the element's centroid. The mesh has a total of 238,892 linear hexahedral elements, with ~5,500 elements in each scaffold.

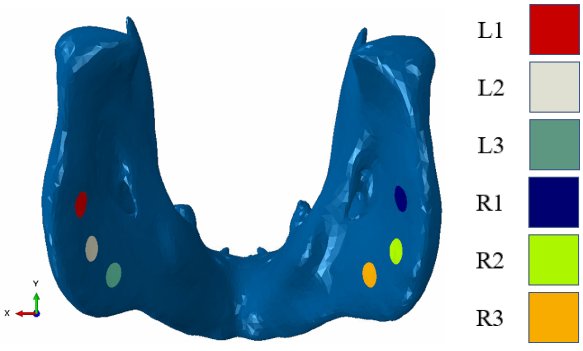

FIGURE 7: A view of the mandible from the rear, with the different scaffolds colored

To estimate the mechanical stimulus that would act on the scaffolds, the finite element elasticity analysis was setup to mimic loads induced by mastication. In general, the chewing action of a pig depends on six muscles: the lateral pterygoid, the medial pterygoid, the masseter, the temporalis, the zygomaticomandibularis and the digastric [49]. A model of the mandible with the loads and boundary conditions is shown in Fig. 8

The muscle forces and activation timings are based on those from [49] with forces adjusted to account for animal size differences [50]. The lines of action of the muscles were estimated based on the muscle origin and insertion points in the CT scan. As pigs alternate between crushing bolus on the left and right, a load case was included for each case. The frequency of each load case was estimated to be 9,800 cycles per day based on [51, 52].

At the temporomandibular joint, a frictionless roller boundary condition is imposed. This prevents translation along the y-axis, but leaves the joint otherwise free to move. A fixed boundary condition is imposed on the most posterior molar to represent the resistance from the food (bolus) being processed. The molar being constrained is alternated between the left and right sides for each mastication load case.

The simulated duration of the mechanobiological simulation for the pig mandible is 24 weeks, or 168 time steps.

4. RESULTS

The design resulting from the optimization process is shown in Fig. 9c. Perhaps its most striking feature is that it is almost rectilinear. The maximum variation in l across the whole scaffold is less than 2%. This represents a substantial deviation from the initial design, which has significant curvature and a widely varying rod-to-rod spacing. Indeed, all of the designs we found from the various starting points were close to rectilinear. We note that, as shown by our previous work on design of rectilinear scaffolds, the orientation has a negligible effect on the scaffold performance [32]. Although we did not perform an exploration of the design space with zero-order methods, the fact that all the optimizations starting from significantly different initial designs converged to similar near-rectilinear designs is an indication that this problem is not highly multimodal. We posit the reason the optimal design is nearly rectilinear is the following. The region of the mandible in which these scaffolds are implanted is a flat bone, whose loading is dominated by the nearby insertions of the masseter and medial pterygoid. Moreover, the scaffolds are small relative to the size of the mandible, hence the stress field through the scaffolds is practically uniform. Also, the direction of these muscles' lines of action are nearly identical in both load cases. Therefore, the stress state in the scaffolds favors a rectilinear design in which rods are aligned with the load direction.

The mass growth of the optimized curvilinear designs is compared to that in a) a rectilinear reference design previously used in in vivo experiments [42], and b) a rectilinear scaffold optimized for the same conditions (see Table 2). The unit cell parameter ranges for all three scaffolds are presented in Table 3. Furthermore, the plots of the final bone density distribution of the reference and optimized curvilinear design are shown in Fig. 10

Both optimized designs outperform the reference design by a

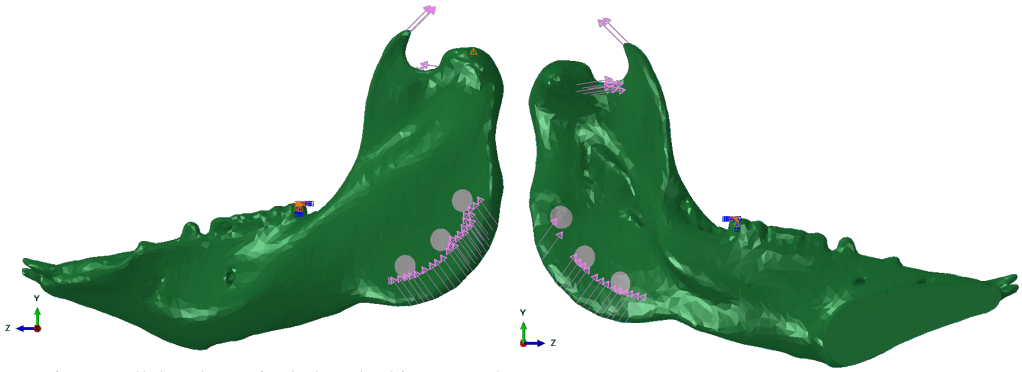

(a) View parallel to the sagittal plane looking towards it

(b) View from the sagittal plane looking out.

FIGURE 8: Mandible with loads and boundary conditions at a point in the mastication cycle. Only half of the mandible is shown for clarity, as the muscle insertions and boundary conditions are considered symmetric. The arrows at the angle of the mandible denote the combined forces of the masseter and medial pterygoid. The arrows located at the coronoid process are the combined temporalis and zygomaticomandibularis muscle forces. The arrows just below the condylar process on the inside of the mandible represent the force from the lateral pterygoid. The orange triangle at the peak of the condylar process represents a roller displacement boundary condition normal to the y-axis. The blue and orange triangles at the molar represent fixed displacement boundary conditions.

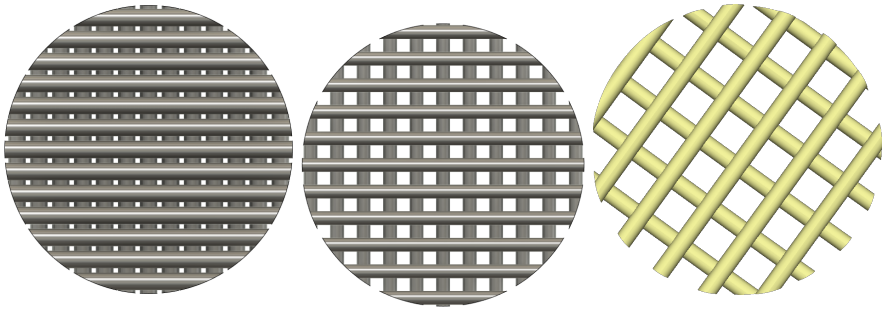

(a) Surrogate model optimized rectilinear

(b) Reference [42]

(c) Optimized curvilinear scaffold

FIGURE 9: Comparison of the optimized curvilinear design to a reference rectilinear design that has been evaluated in-vivo [42] and a rectilinear design optimized using the previously reported surrogate-based method. Note that the orientation of the scaffolds in the figure is not indicative of their orientation at implantation

Scaffold Position	Reference [42] (%)	Optimized Rectilinear (%)	Optimized Curvilinear (%)
L1	32.9	45	47.2
L2	31	48	48.9
L3	48.2	64.6	62.3
R1	32.2	45.1	45.6
R2	30.9	50.5	48.3
R3	53.3	68.6	64.5

TABLE 2: Mass growth percentages of each design in each scaffold position.

Design	α	d/l	p_s (μm)
Reference	0.18	0.523	359
Rectilinear	0.2	0.8	122
Curvilinear	0.3975	0.351-0.357	878-902

TABLE 3: Scaffold design parameters. Note that the curvilinear d/l and p_s values are not constant across the scaffold, so ranges are given.

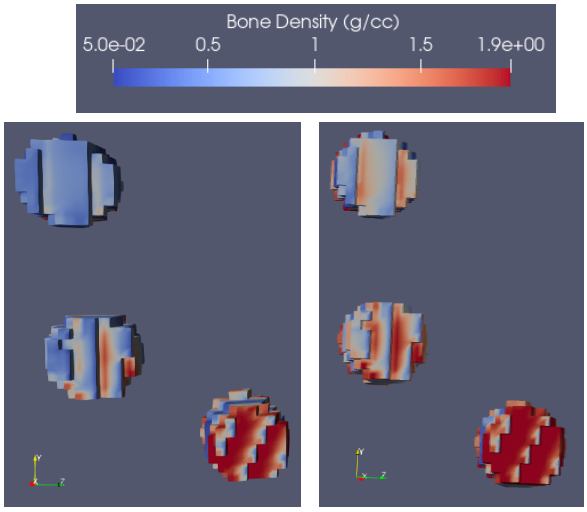

(a) Reference **(b)** Optimized curvilinear

FIGURE 10: Final bone density distributions in the reference and curvilinear optimized scaffolds. The left and right side bone density distributions are very similar, so only scaffolds R1, R2 and R3 are shown

large margin. From Fig. 10, it can be observed that the curvilinear design has a greater final bone density throughout all the scaffolds. However, the curvilinear optimized design and rectilinear optimized design have nearly identical performance in terms of mass growth. It is unlikely this performance difference would be noticeable in vivo. It is interesting that the two optimizations did not converge to the same design. The optimized rectilinear design has a larger d/l and smaller pores than anywhere in the curvilinear design (see Table 3). This suggests the existence of at least two local optima, though it is possible the surrogate optimized scaffold optima is an artefact of the surrogate model and not present in the actual system response.

5. CONCLUSIONS

This paper introduced a computational technique to design curvilinear scaffolds made by DIW to maximize bone growth, as determined by a mechanobiological simulation of bone adaptation. The optimized curvilinear design was found to exceed the bone growth of a reference design previously used for in vivo studies, and it exhibits similar bone growth to that of a rectilinear design optimized with the surrogate model based approach of [32]. While in the example presented here the optimal scaffold turned out to be nearly rectilinear, scaffolds subject to more complex loading conditions could benefit from the additional design freedom.

The method presented here can generate arbitrarily complex curvilinear geometries through the addition of more radial basis functions. The use of the thin-plate spline RBFs to define level sets ensures smooth, continuously varying rod contours that facilitate deposition. Moreover, the method can readily support the necessary geometric constraints to ensure the optimal design can be manufactured using existing DIW technology. Furthermore, the compact design representation and the parallel finite-difference approach can efficiently exploit HPC systems to reduce the wall-time of the gradient-based optimization when compared to using analytical sensitivities.

Several important aspects of bone scaffold design are not considered in this study and will be addressed in future research. Resorption of both the bone and scaffold are not considered here, which is necessary to understand the long-term behavior of the scaffold-bone system. Moreover, the stresses within the scaffold are not considered, making the scaffold's ability to withstand in-vivo loads unknown. Incorporation of these considerations will help increase the clinical viability of bone scaffolds.

6. ACKNOWLEDGMENTS

Support from the National Science Foundation, award CMMI-1727591 to conduct this work is gratefully acknowledged. We would also like to thank Prof. Mariana Kersh at the University of Illinois at Urbana-Champaign for useful discussions on this subject.

REFERENCES

[1] Finkemeier, C. G., 2002. "Bone-Grafting and Bone-Graft Substitutes". *Journal of Bone and Joint Surgery,* ***84-A***(3), pp. 454–464.

[2] Dimitriou, R., Jones, E., McGonagle, D., and Giannoudis, P. V., 2011. "Bone regeneration: current concepts and future directions". *BMC Medicine,* ***9***(66).

[3] Khan, S. N., Cammisa, F. P., Sandhu, H. S., Diwan, A. D., Girardi, F. P., and Lane, J. M., 2005. "The biology of bone grafting.". *The Journal of the American Academy of Orthopaedic Surgeons,* ***13***(1), pp. 77–86.

[4] Brydone, A. S., Meek, D., and MacLaine, S., 2010. "Bone grafting, orthopaedic biomaterials, and the clinical need for bone engineering". In Proceedings of the Institution of Mechanical Engineers, Part H: Journal of Engineering in Medicine, Vol. 224, pp. 1329–1343.

[5] Wang, W., and Yeung, K. W. K., 2017. "Bone grafts and biomaterials substitutes for bone defect repair: A review". *Bioactive Materials,* ***2***(4), pp. 224–247.

[6] Lauthe, O., Soubeyrand, M., Babinet, A., Dumaine, V., Anract, P., and Biau, D. J., 2018. "The indications and donor-site morbidity of tibial cortical strut autografts in the management of defects in long bones". *Bone and Joint Journal,* ***100B***(5), pp. 667–674.

[7] Amini, A. R., Laurencin, C. T., and Nukavarapu, S. P., 2012. "Bone tissue engineering: Recent advances and challenges". *Critical Reviews in Biomedical Engineering,* ***40***(5), pp. 363–408.

[8] Metz, C., Duda, G. N., and Checa, S., 2019. "Towards multi-dynamic mechano-biological optimization of 3D-printed scaffolds to foster bone regeneration.". *Acta biomaterialia,* ***101***, pp. 117–127.

[9] Carter, D. R., and Beaupré, G. S., 2001. *Skeletal Function and Form: Mechanobiology of Skeletal Development, Aging, and Regeneration*. Cambridge University Press, New York.

[10] Adachi, T., Osako, Y., Tanaka, M., Hojo, M., and Hollister, S. J., 2006. "Framework for optimal design of porous scaffold microstructure by computational simulation of bone regeneration". *Biomaterials,* ***27***(21), pp. 3964–3972.

[11] Christen, P., Ito, K., Ellouz, R., Boutroy, S., Sornay-Rendu, E., Chapurlat, R. D., and Van Rietbergen, B., 2014. "Bone remodelling in humans is load-driven but not lazy". *Nature Communications,* ***5***(4855).

[12] Giannoudis, P. V., Einhorn, T. A., and Marsh, D., 2007. "Fracture Healing: The diamond concept". *Injury,* ***38***(S4), pp. S3—-S6.

[13] Soballe, K., Hansen, E. S., Brockstedt-Rasmussen, H., and Bunger, C., 1993. "Hydroxyapatite coating converts fibrous tissue to bone around loaded implants". *Journal of Bone and Joint Surgery - Series B,* ***75***(2), pp. 270–278.

[14] Almeida, H. A., and Bártolo, P. J., 2014. "Design of tissue engineering scaffolds based on hyperbolic surfaces: Structural numerical evaluation". *Medical Engineering and Physics,* ***36***(8), pp. 1033–1040.

[15] Wieding, J., Wolf, A., and Bader, R., 2014. "Numerical optimization of open-porous bone scaffold structures to match the elastic properties of human cortical bone". *Journal of the Mechanical Behavior of Biomedical Materials,* ***37***, pp. 56–68.

[16] Dias, M. R., Guedes, J. M., Flanagan, C. L., Hollister, S. J., and Fernandes, P. R., 2014. "Optimization of scaffold design for bone tissue engineering: A computational and experimental study". *Medical Engineering and Physics,* ***36***(4), apr, pp. 448–457.

[17] Mohammed, M. I., and Gibson, I., 2018. "Design of Three-Dimensional, Triply Periodic Unit Cell Scaffold Structures for Additive Manufacturing". *Journal of Mechanical Design, Transactions of the ASME,* ***140***(7), pp. 1–10.

[18] Roberge, J., and Norato, J., 2018. "Computational design of curvilinear bone scaffolds fabricated via direct ink writing". *CAD Computer Aided Design,* ***95***, pp. 1–13.

[19] Luo, D., Rong, Q., and Chen, Q., 2017. "Finite-element design and optimization of a three-dimensional tetrahedral porous titanium scaffold for the reconstruction of mandibular defects". *Medical Engineering & Physics,* ***47***, sep, pp. 176–183.

[20] Sutradhar, A., Paulino, G. H., Miller, M. J., and Nguyen, T. H., 2010. "Topological optimization for designing patient-specific large craniofacial segmental bone replacements". *Proceedings of the National Academy of Sciences,* ***107***(30), jul, pp. 13222–13227.

[21] Makowski, P., and Kuś, W., 2016. "Optimization of bone scaffold structures using experimental and numerical data". *Acta Mechanica,* ***227***(1), pp. 139–149.

[22] Blázquez-Carmona, P., Sanz-Herrera, J. A., Martínez-Vázquez, F. J., Domínguez, J., and Reina-Romo, E., 2021. "Structural optimization of 3D-printed patient-specific ceramic scaffolds for in vivo bone regeneration in load-bearing defects". *Journal of the Mechanical Behavior of Biomedical Materials,* ***121***(May).

[23] Egan, P. F., Ferguson, S. J., and Shea, K., 2017. "Design of Hierarchical Three-Dimensional Printed Scaffolds Considering Mechanical and Biological Factors for Bone Tissue Engineering". *Journal of Mechanical Design, Transactions of the ASME,* ***139***(6), pp. 1–9.

[24] Egan, P. F., Bauer, I., Shea, K., and Ferguson, S. J., 2019. "Mechanics of Three-Dimensional Printed Lattices for Biomedical Devices". *Journal of Mechanical Design, Transactions of the ASME,* ***141***(3), pp. 1–12.

[25] Byrne, D. P., Lacroix, D., Planell, J. A., Kelly, D. J., and Prendergast, P. J., 2007. "Simulation of tissue differentiation in a scaffold as a function of porosity, Young's modulus and dissolution rate: Application of mechanobiological models in tissue engineering". *Biomaterials,* ***28***(36), dec, pp. 5544–5554.

[26] Sanz-Herrera, J. A., Garcia-Aznar, J. M., and Doblare, M., 2008. "A mathematical model for bone tissue regeneration inside a specific type of scaffold". *Biomechanics and Modeling in Mechanobiology,* ***7***(5), pp. 355–366.

[27] Bashkuev, M., Checa, S., Postigo, S., Duda, G., and Schmidt, H., 2015. "Computational analyses of different intervertebral cages for lumbar spinal fusion". *Journal of Biomechanics,* ***48***(12), sep, pp. 3274–3282.

[28] Pobloth, A. M., Checa, S., Razi, H., Petersen, A., Weaver, J. C., Chmidt-Bleek, K., Windolf, M., Tatai, A. A., Roth,

C. P., Schaser, K. D., Duda, G. N., and Schwabe, P., 2018. "Mechanobiologically optimized 3D titanium-mesh scaffolds enhance bone regeneration in critical segmental defects in sheep". *Science Translational Medicine,* ***10***(423).

[29] Paris, M., Götz, A., Hettrich, I., Bidan, C. M., Dunlop, J. W. C., Razi, H., Zizak, I., Hutmacher, D. W., Fratzl, P., Duda, G. N., Wagermaier, W., and Cipitria, A., 2017. "Scaffold curvature-mediated novel biomineralization process originates a continuous soft tissue-to-bone interface". *Acta Biomaterialia,* ***60***, pp. 64–80.

[30] Wu, C., Fang, J., Entezari, A., Sun, G., Swain, M. V., Xu, Y., Steven, G. P., and Li, Q., 2021. "A time-dependent mechanobiology-based topology optimization to enhance bone growth in tissue scaffolds". *Journal of Biomechanics,* ***117***, p. 110233.

[31] Boccaccio, A., Fiorentino, M., Uva, A. E., Laghetti, L. N., and Monno, G., 2018. "Rhombicuboctahedron unit cell based scaffolds for bone regeneration: geometry optimization with a mechanobiology driven algorithm". *Materials Science and Engineering C,* ***83***(March 2017), pp. 51–66.

[32] Cohen, D. O., Aboutaleb, S. M. G., Johnson, A. W., and Norato, J. A., 2021. "Bone Adaptation-Driven Design of Periodic Scaffolds". *Journal of Mechanical Design*.

[33] Donato, G., and Belongie, S., 2002. "Approximate Thin Plate Spline Mappings". pp. 21–31.

[34] Simeunović, A., and Hoelzle, D. J., 2020. "Nonlinear and linearized gray box models of direct-write printing dynamics". *Rapid Prototyping Journal,* ***26***(10), pp. 1665–1676.

[35] Lan Levengood, S. K., Polak, S. J., Wheeler, M. B., Maki, A. J., Clark, S. G., Jamison, R. D., and Wagoner Johnson, A. J., 2010. "Multiscale osteointegration as a new paradigm for the design of calcium phosphate scaffolds for bone regeneration". *Biomaterials,* ***31***(13), may, pp. 3552–3563.

[36] Hoelzle, D. J., Alleyne, A. G., and Wagoner Johnson, A. J., 2008. "Micro-robotic deposition guidelines by a design of experiments approach to maximize fabrication reliability for the bone scaffold application". *Acta Biomaterialia,* ***4***(4), pp. 897–912.

[37] Wright, G. B., 1997. "Radial Basis Function Interpolation : Numerical and Analytical Developments". PhD thesis, University of Colorado.

[38] Buhmann, M. D., 2003. *Radial Basis Functions: Theory and Implementations*. Cambridge Monographs on Applied and Computational Mathematics. Cambridge University Press.

[39] Harker, M., and O'leary, P., 2015. "Regularized reconstruction of a surface from its measured gradient field". *Journal of Mathematical Imaging and Vision,* ***51***(1), pp. 46–70.

[40] Jacobs, C. R., 1994. "Numerical simulation of bone adaptation to mechanical loading". PhD thesis, Stanford University.

[41] Beyer, W. A., Fawcett, L. R., Hartem, L. P., and Swartz, B. K., 1992. "The volume common to two congruent circular cylinders". *Journal of Symbolic Computation,* ***13***(2), pp. 221–230.

[42] Polak, S. J., Levengood, S. K., Wheeler, M. B., Maki, A. J., Clark, S. G., and Johnson, A. J., 2011. "Analysis of the roles of microporosity and BMP-2 on multiple measures of bone regeneration and healing in calcium phosphate scaffolds". *Acta Biomaterialia,* ***7***(4), apr, pp. 1760–1771.

[43] Arndt, D., Bangerth, W., Blais, B., Clevenger, T. C., Fehling, M., Grayver, A. V., Heister, T., Heltai, L., Kronbichler, M., Maier, M., Munch, P., Pelteret, J.-P., Rastak, R., Thomas, I., Turcksin, B., Wang, Z., and Wells, D., 2020. "Deal.ii -9.2.0". *Journal of Numerical Mathematics,* ***28***, pp. 131–146.

[44] Trilinos-Project-Team, and Triinos-Project-Team, 2021. The Trilinos Project.

[45] Hyperworks, 2017. Hyperwork 2017.3.

[46] Liu, Z. J., and Herring, S. W., 2000. "Masticatory Strains on Osseous and Ligamentous Components of the Temporomandibular Joint in Miniature Pigs". *Journal of Orofacial Pain,* ***14***(4), pp. 265–278.

[47] Virtanen, P., Gommers, R., Oliphant, T. E., Haberland, M., Reddy, T., Cournapeau, D., Burovski, E., Peterson, P., Weckesser, W., Bright, J., van der Walt, S. J., Brett, M., Wilson, J., Millman, K. J., Mayorov, N., Nelson, A. R. J., Jones, E., Kern, R., Larson, E., Carey, C. J., Polat, b., Feng, Y., Moore, E. W., VanderPlas, J., Laxalde, D., Perktold, J., Cimrman, R., Henriksen, I., Quintero, E. A., Harris, C. R., Archibald, A. M., Ribeiro, A. H., Pedregosa, F., van Mulbregt, P., and SciPy 1.0 Contributors, 2020. "{SciPy} 1.0: Fundamental Algorithms for Scientific Computing in Python". *Nature Methods,* ***17***, pp. 261–272.

[48] , 2016. Amira.

[49] Langenbach, G. E. J., Zhang, F., Herring, S. W., and Hannam, A. G., 2002. "Modelling the masticatory biomechanics of a pig". *Journal of Anatomy,* ***201***(5), pp. 383–393.

[50] Biewener, A. A., 2005. "Biomechanical consequences of scaling". *Journal of Experimental Biology,* ***208***, 5, pp. 1665–1676.

[51] Bigelow, J. A., and Houpt, T. R., 1988. "Feeding and drinking patterns in young pigs". *Physiology and Behavior,* ***43***(1), pp. 99–109.

[52] Herring, S. W., 1976. "The Dynamics of Mastication in Pigs". *Archives of Oral Biology,* ***21***, pp. 473–480.